Seismic detection of a low-velocity layer atop the 410-km discontinuity: verification of an electromagnetically detected layer of partial-melt atop the 410-km discontinuity beneath SE Arizona

A Senior Project
presented to
the Faculty of the Physics Department
California Polytechnic State University, San Luis Obispo

In Partial Fulfillment
of the Requirement for the Degree
Bachelor of Science

by
Dwight W. Townsend
May 2012

Seismic detection of a low-velocity layer atop the 410-km discontinuity: verification of an electromagnetically detected layer of partial-melt atop the 410-km discontinuity beneath SE Arizona.

by Dwight W. Townsend and John J. Jasbinsek

Abstract

Receiver functions calculated from a ten-station subset of the Earthscope Transportable Array (TA) show a well-defined 45 km thick low-velocity layer atop the 410-km discontinuity ("410") beneath the Tucson, Arizona, region. This observation is consistent with a previously detected layer of increased electrical conductivity in the same region, from which the existence a 5-30 km thick layer of partial melt atop the 410 was inferred. Relative to IASP91 the low-velocity layer is characterized with respect to increasing depth as: a 3.4% shear wave velocity decrease over a 10-km interval, underlain by a 25-km thick constant velocity interval, followed by a diffuse 30 km thick bottom gradient over which the shear wave velocity increases by 3.5%. The shear wave velocity increase over the bottom interval is less than predicted by the IASP91 earth model, suggesting the olivine-wadsleyite transformation takes place in water-saturated conditions. The diffuse bottom gradient is consistent with a hydrated mantle transition zone, thus the low-velocity layer is interpreted as a manifestation of the Transition Zone Water Filter model.

Introduction

Earth's Mantle

Earth's mantle, bounded by the crust and core, spans depths of approximately 35 km to 2,900 km (Fig. 1) and contains 80% percent of Earth's volume and 65% of its mass (Helffrich and Wood 2001). The mineralogy of Earth's mantle is commonly approximated by the pyrolite model (Fig. 2) (Jackson 1998).

Seismic velocities in the mantle increase smoothly with mantle depth (Fig. 2) however two distinct changes in seismic wave-velocity, or seismic discontinuities, occur at depths of 410 and 660km, which bound the Mantle Transition Zone (MTZ) (Fig. 2). These seismic velocity discontinuities are called the 410- and 660-km seismic discontinuities, and are termed the "410" and the "660" in the following. The origin of the 410 and 660 are explained by phase changes of the mantle material (Helffrich and Wood 2001). At the 410-km, olivine $(Mg, Fe)_2SiO_4$ undergoes a

pressure induced (~13 GPa) phase transformation to become a more compact compound called wadsleyite through which seismic waves propagate at a higher velocity (Fig. 2). Similarly, at the depth of 520 km and a pressure of ~18 GPa wadsleyite undergoes a phase change to become ringwoodite. A seismic wave velocity discontinuity for this phase transition is not globally detected (Shearer 1996) and thus not all global seismic velocity models include this velocity step (Fig. 2). At 660 km depth (~23 GPa) ringwoodite undergoes a disassociation reaction, becoming perovskite, $(Mg,Fe)SiO_3$, and magnesiowüstite, $(Mg,Fe)O$ (Jackson 1998; Helffrich and Wood 2001).

Geochemical observations and style of mantle convection

A longstanding problem in geochemistry is the discrepancy the rare-earth element compositions between mid-ocean ridge basalt (MORB) and ocean island basalt (OIB) (Fig. 3) (Bercovici and Karato 2003). Originally, a model of layered mantle convection containing distinct and un-mixing geochemical reservoirs was proposed to explain the geochemical differences (Fig. 4a). In the layered convection model, MORB is generated from shallow mantle sources and is depleted in incompatible elements such as Uranium and Thorium, while OIB is derived from deep mantle sources below the MTZ and is not depleted in incompatible elements (Fig. 3, 5). However seismic tomography suggests that subducted oceanic lithosphere may occasionally reach the core-mantle boundary and so a purely layered mantle convection model is unlikely (Fig. 6). Thus at the other end of the spectrum some form of whole mantle convection is supported by the geophysical data, suggesting that longstanding isolated chemical reservoirs are unlikely.

More recently, a new model of mantle convection has been proposed to reconcile mantle convection models with the geochemical observations: the Transition Zone Water Filter model (TZWF) (Bercovici and Karato 2003). The TZWF crucially relies upon the difference in water solubility of the olivine and wadsleyite phases. Olivine can incorporate up to 1 wt% water (as OH^- and H^-) whereas wadsleyite can incorporate up to 2.7 wt% water (van der Lee and Wiens 2006). The TZWF model is schematically shown in Figure 5. Upwelling wadsleyite from the MTZ upon crossing the 410 undergoes a phase transformation to olivine. If the amount of water in the wadsleyite is greater than the saturation level for olivine, then partial melting will occur in the olivine due to the decreased melting temperature of the hydrated olivine phase. The partial melt is hypothesized to have neutral buoyancy between the upper mantle assemblage and the MTZ and thus pools atop the 410 (Bercovici and Karato 2003). The melt layer will also entrain incompatible elements such as Uranium and Thorium (Fig. 3), and thus dynamically alter the geochemical signature of the upper mantle, which in the TZWF model, continues to rise into the upper mantle and becomes MORB source. In contrast, OIB is posited to arise at the surface via mantle plumes, which rise at a much greater rate than ambient mantle upwelling and thus retain the chemical signature of its deep mantle source (Fig. 5).

The origin of water in the mantle is a subject of considerable debate. Some primordial water from the original accretion of the earth surely resides in the mantle. Dehydration from subducting oceanic slabs into the mantle transition zone can release some amount of water into the mantle transition zone, although which mineral phases and how much water survives in the slab to transition zone depths is not fully understood (Hirschmann, Aubaud et al. 2005; Courtier and Revenaugh 2006; van der Lee and Wiens 2006; Richard and Bercovici 2009). However it is beyond the scope of this study to evaluate all the proposed mechanisms for the hydration and distribution of water in the mantle transition zone, and it is simply noted that it is possible for significant amounts of water (1-10 ocean masses) to reside in the mantle.

An attractive feature of the TZWF model is its dynamic method of altering mantle geochemistry and satisfying the constraints imposed by the observed geochemistry of MORB and OIB. In addition, the model strikes a compromise between layered and whole mantle convection models: mantle layers, such as the 410, remain fundamentally important yet subducting slabs and rising mantle plumes retain the main features of whole mantle convection (Fig. 4, 5).

The TZWF is also attractive to seismologists because it creates a testable hypothesis: existence of a sufficiently thick melt layer atop the 410 would be detectable as a layer of low seismic velocity. A previous study of electromagnetic data beneath the Tucson region of SE Arizona previously detected a region of high electrical conductivity and interpreted the data as consistent with the TZWF model (Toffelmier and Tyburczy 2007). In this study receiver functions calculated from a ten-station subset of the Earthscope Transportable Seismic Array (TA) are analyzed to determine if a layer of low velocity atop the 410 can be confirmed with an independent geophysical method.

Methods

What is a receiver function?

A receiver function (RF) is a time-series of P-to-S wave mode conversions at internal earth boundaries such as the crust-mantle boundary (Moho), and the 410- and 660-km seismic discontinuities (Fig. 7). An earth boundary with a sufficiently large contrast in seismic properties (compressional, P, and shear, S, wave speeds) over a sufficiently sharp depth interval will convert detectable energy from P to S waves. This P-to-S conversion at some depth d (denoted P_dS) can be detected at 3-component seismic stations by deconvolving the vertical seismic channel, where P-waves are dominantly polarized, from the horizontal seismic channels where S-waves are dominantly polarized (Vinnik 1977). Thus P_ds conversions are recorded on the horizontal channels. After deconvolution, the resulting waveform is a composite of P-to-S conversions below the station. A cartoon of receiver functions and P-to-S conversion is shown in Figure 7.

Calculation of receiver functions

P-to-S conversions have maximal amplitude on the radial channel of the seismometer. In order to maximize the P-to-S response, a rotation of the three channels from Vertical (Z), North (N), and East (E) to Vertical (Z), Radial (R), and Tangential (T) is performed. The earthquake source wave is approximated as the P-wave response on the vertical (Z) channel of the seismometer.

The seismogram is assumed to be a convolution between the earthquake source function and earth's reflectivity/layer structure (RS). The receiver function, RF, is then the approximated reflectivity structure, which can be obtained by deconvolution. In this study, the deconvolution was performed in the spectral domain via with "water-level" regularization (Fig. 7).

To solve for the RS we use a Fourier transform, which changes convolution in the time domain to multiplication in frequency domain. The vertical channel is divided into the radial (spectral division) and the inverse Fourier Transform is applied to return to the time domain. Mathematically, for every source-receiver pair the calculation of a receiver function is carried out as:

$$Z * RS = R$$

$$F[Z * RS] = F[R]$$

$$F[Z] \cdot F[RS] = F[R]$$

$$F[RS] = \frac{F[R]}{F[Z]}$$

$$RF = RS \sim \frac{F[R]}{F[Z] + "water - level"}$$

Data Processing

The location of the seismic stations is shown in Figure 8 and the location of earthquake sources relative to the stations is shown in Figure 9. Earthquakes were selected from the SE back-azimuth (South America). In total 69 earthquakes with body-wave magnitude > 5.4 were selected. Receiver functions were computed at each station, and obviously spurious data (e.g. highly oscillatory) were discarded. Data were then corrected for distance from source to receivers (move-out correction) to allow stacking and mapped from the time domain to the depth domain with the IASP91 velocity model. The data were linearly stacked to enhance common signal and to form a mean receiver function, against which individual receiver functions were cross-correlated. Traces with positive cross-correlation were retained and re-stacked to from a final receiver function trace (Fig. 10).

Modeling

The receiver function stack shows a clear positive polarity $P_{410}s$ and $P_{660}s$ arrival from the mantle transition zone (Fig. 10). This is expected because the phase transformations responsible for the 410 and 660 are global features. Noteworthy is the prominent negative polarity P_ds arrival just above and interfering with $P_{410}s$ (Fig. 10). Because the polarity is reversed with respect to $P_{410}s$ this arrival may be produced by a low velocity layer atop the 410. To assess if such a low-velocity layer is required by the data, the final receiver function stack was modeled with a five-parameter set of velocity models which include both low-velocity layer and non-low-velocity layer models (Fig 11, Table 1). The five parameters are: top gradient thickness, TG; bottom gradient thickness, BG; a constant velocity slab thickness, ST; shear-wave velocity reduction in the top gradient, dV_s-TG; shear-wave velocity increase in the bottom gradient, dV_s-BG (Fig. 11, Table 1). These velocity models are termed Double Gradient Slab models (DGS) .The resulting 116,160 velocity models were used to calculate synthetic receiver functions from the average observed P-wave response of the data. The observed stacked receiver function (Fig. 10) was cross-correlated to the 116,160 synthetic receiver functions in a depth interval surrounding the 410 to find the maximum likelihood DGS model.

The fit of each synthetic receiver function is quantified by a Gaussian likelihood function

$$L(m) = \exp\left(-\frac{1}{2}(d - g(m))^T C_D^{-1} \left(d - g(m)\right) \right).$$

Here **d** is the observed RF stack, **g(m)** is a synthetic RF, $\mathbf{C_D}$ is the data covariance matrix. The probability of a DGS model, **m**, given a data vector **d**, is $P(m \mid d) = \rho(m) L(m \mid d)$. The factor $\rho(m)$ allows the assignment of an a priori model distribution. Here, each model is considered equally likely thus $\rho(m) \equiv 1$ (Sambridge 1999).

From the 5-dimensional volume of model fit, 1- and 2-dimensional probability distributions for model fit can be calculated as

$$M_1(m_i) = \int \ldots \int P(m) \prod_{\substack{k=1 \\ k \neq i}}^{d} dm_k \ ,$$

where d is the number of model parameters (5). Two dimensional marginal probability distributions are similarly defined:

$$M_2(m_i, m_j) = \int \ldots \int P(m) \prod_{\substack{k=1 \\ k \neq i,\, j}}^{d} dm_k \ .$$

The 1- and 2-D marginal probability distribution plots allow a visual assessment of the tradeoffs in model parameters. Peak values in the 1-D marginal probability

distributions indicate the most probable model parameters, and the 2-d marginal probability distributions show the tradeoffs to model fit between any pair of model parameters.

Results

Figure 12 shows the best fitting synthetic receiver function to the observed receiver function stack. The fit is within the standard error bars around the observed receiver function stack. The 1- and 2-dimensional marginal probability distributions indicate that the observed receiver function is reasonably well constrained by the modeling process (Fig. 13). The bottom gradient thickness parameter (BG) is very well constrained as seen by the compact peak in the 1-D marginal probability distribution. Although the top gradient thickness (TG) is not well constrained the shear-wave velocity reduction, dV_s-TG, in the top gradient is well constrained. This is further seen in the vertically oriented 2-dimensional marginal probability distribution of the parameters TG and dV_s-TG. The bottom gradient thickness, BG, and the bottom gradient shear-velocity jump, dV_s-BG, are tightly constrained as evidenced in the corresponding 1-dimensional marginal probability distributions, and the corresponding 2-dimensional marginal probability distribution (Fig. 13). The constant velocity slab thickness (ST) contains a distinct peak at 30 km, however the decay of the probability distribution is slow and thus ST is not very tightly constrained.

Even though not all five modeling parameters are tightly constrained, there *must* be a velocity reduction (dVs-TG >0) atop the 410-km (Fig. 13). This velocity reduction is required by the data with 100% probability. The best-fitting DGS model to the data is: TG = 10 km; BG = 30 km; ST = 25 km; dVs-TG = -0.16 km/s; dVs-BG = 0.17 km/s. The layer of low-velocity found here will be referred to as the 410 Low Velocity Layer (410-LVL).

The thickness of the low-velocity layer atop the 410 is estimated to be 45 km thick (ST plus half of TG plus BG) and requires a shear-wave velocity reduction of -0.16 km/s, or 3.4% relative to the IASP91 earth model. The diffuse characteristic of the parameter BG is also well constrained, suggesting that the transition from the low-velocity layer to the olivine-wadsleyite phase transformation is not sharp.

Discussion

The results confirm the existence of low-velocity layer atop the 410-km seismic discontinuity beneath the Tucson region of SE Arizona as previously found with electromagnetic methods (Toffelmier and Tyburczy 2007). The confirmation of the low-velocity layer with an independent geophysical method provides great confidence that the low-velocity layer indeed exists in this region. The present modeling results indicate an approximately 45 km thick layer, significantly larger than the 5-30 km layer suggested by the electromagnetic study. The resolution of the near-vertical seismic data through the 410 likely provides a more robust

thickness estimate than the electromagnetic data modeling results. In addition, the seismic modeling here provides a shear-wave velocity reduction estimate of 3.4% through the low-velocity layer. The results of the electromagnetic study indicate a conductance of 3 x 10^4 S. Unfortunately, no relationship between conductance of partially melted olivine at high pressures and seismic velocity is known to correlate these the conductance and shear-wave velocity data.

Previous seismic studies using receiver functions and triplicated waves have detected low-velocity layers atop the 410 in many regions, yet the regions are geographically isolated, suggesting the low-velocity layers are not a global phenomenon (Fee and Dueker 2004; Song, Helmberger et al. 2004; Jasbinsek and Dueker 2007; Vinnik and Farra 2007). The thickness and velocity reductions found here fall within the boundaries established by previous seismic observations.

The correlation of the low-velocity layer with a diffuse olivine-wadsleyite transition interval (i.e. the 410-km discontinuity) provides a clue to interpreting its origin. Mineral physics studies of the olivine-wadsleyite phase transformation indicate that in the presence of water (OH^- and H^+) the phase transformation will (1) occur over a broader depth interval, and (2) occur at somewhat shallower depths (Smyth and Frost 2002). With BG = 25 km, the modeling results clearly indicate a broad olivine wadsleyite transition (Fig. 13). Because the 410-LVL produces such a P_ds signal equal in magnitude to $P_{410}s$, it is suggested that the water content of the wadsleyite exceeds the saturation level of olivine (0.9 wt%). This observation is consistent with the requirements of the TZWF model. However, the $P_{410}s$ signal appears deep instead of shallow. This result is not predicted by the TZWF model, and may be due to a non-equilibrium phase transformation (Solomatov and Stevenson 1994).

Conclusions

A low-velocity layer atop the 410-km seismic discontinuity was found using receiver functions calculated at ten 3-component seismic stations in the southeast region of Arizona near Tucson. A broad 410-km discontinuity in the data is consistent with the presence of water in the mantle transition zone, thus the low velocity layer is interpreted caused by partial melt as predicted by the Transition Zone Water Filter model. The layer of partial melt is 45 km thick with a 3.4% shear velocity reduction and diffuse 410 phase transformation. The seismic results here corroborate an electromagnetic study of the same region that interpreted enhanced electrical conductivity as evidence for a layer of partial melt resulting from local operation of the TZWF model.

References

Bercovici, D. and S. Karato (2003). "Whole-mantle convection and the transition-zone water filter." Nature **425**: 39-44.

Courtier, A. M. and J. Revenaugh (2006). "A Water-Rich Transition Zone Beneath the Eastern United States and Gulf of Mexico From Multiple ScS Reverberations." Earth's Deep Water Cycle **AGU Geophysical Monograph 168**.

Fee, D. and K. Dueker (2004). "Mantle transition zone topogaphy and structure beneath the Yellowstone hotspot." Geophysical Research Letters **31**: L18603.

Helffrich, G. R. and B. J. Wood (2001). "The Earth's mantle." Nature **412**(6846): 501-507.

Hirschmann, M. M., C. Aubaud, et al. (2005). "Storage capacity of H2O in nominally anhydrous minerals in the upper mantle." Earth and Planetary Science Letters **236**(1-2): 167-181.

Jackson, I. (1998). The Earth's Mantle. Composition, Structure, and Evolution, Cambridge.

Jasbinsek, J. and K. G. Dueker (2007). "Ubiquitous low-velocity layer atop the 410-km discontinuity in the northern Rocky Mountains." Geochemistry Geophysics Geosystems **8, 10**(10).

Richard, G. and D. Bercovici (2009). "Water-induced convection in the Earth's mantle transition zone." Journal of Geophysical Research B: Solid Earth **114**: doi: 10.1029/2008JB005734.

Sambridge, M. (1999). "Geophysical inversion with a Neighbourhood Algorithm - II." Geophysical Journal International **138**: 727-746.

Shearer, P. M. (1996). "Transition zone velocity gradients and the 520-km discontinuity." Journal of Geophysical Research **101**(B2): 3053-3066.

Smyth, J. R. and D. J. Frost (2002). "The effect of water on the 410-km discontinuity: an experimental study." Geophys. Res. Lett. **29**: doi:10.1029/2001GL014418.

Solomatov, V. S. and D. J. Stevenson (1994). "Can sharp seismic discontinuities be caused by non-equilibrium phase transformations?" Earth and Planetary Science Letters **125**(1-4): 267-279.

Song, T. A., D. V. Helmberger, et al. (2004). "Low velocity zone atop the 410 seismic discontinuity in the northwestern United States." Nature **427**: 530-533.

Toffelmier, D. A. and J. A. Tyburczy (2007). "Electromagnetic detection of a 410-km-deep melt layer in the southwestern United States." Nature **447**(7147): 991-994.

van der Lee, S. and D. A. Wiens (2006). "Seismological constraints on Earth's deep water cycle." AGU Geophysical Monongraph. Earth's Deep Water Cycle **168**.

Vinnik, L. (1977). "Detection of waves converted from P to SV in the mantle." Physics of the Earth and Planetary Interiors **15**: 39-45.

Vinnik, L. and V. Farra (2007). "Low S velocity atop the 410-km discontinuity and mantle plumes." Earth and Planetary Science Letters **262**(3-4): 398-412.

Figure Captions

Figure 1. Simplified Earth Cross Section.
Earth's primary divisions: oceanic and continental crust (up to 50 km) depth, mantle (2900 km) depth, outer-core (5100 km depth), and inner-core (6370 km depth). Source:http://www.diercke.com/kartenansicht.xtp?artId=978-3-14-100790-9&stichwort=schema&fs=1

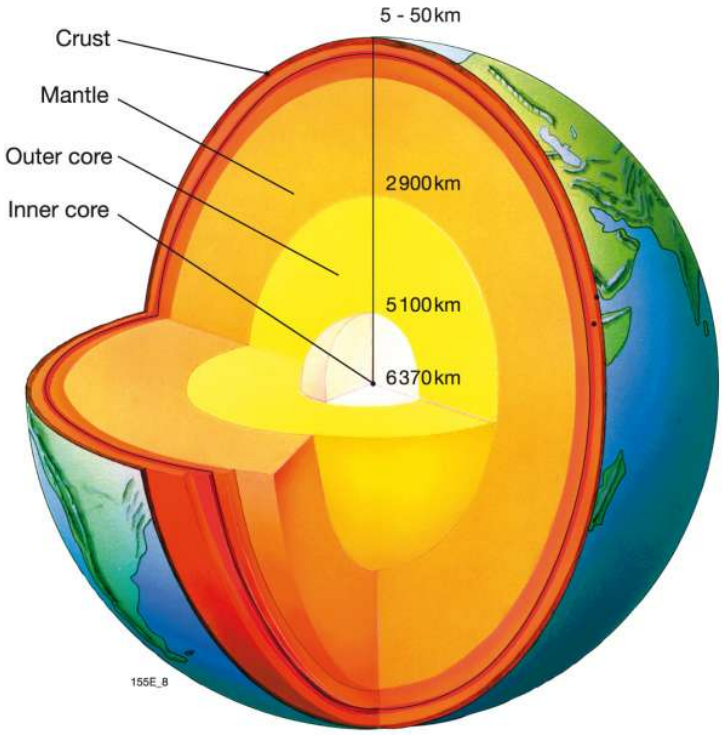

Figure 2. Earth velocity model and mantle mineralogy.
Left: Density, S-wave velocity, and P-wave velocity as a function of depth. Right: Mantle mineralogy and relative proportions as a function of depth. The mantle transition zone is bounded by the velocity steps at 410- and 660-km which are caused by a phase transformation at 410 and a disassociation reaction at 660. The 520-km velocity step in seismic velocity is not globally observed. Source: http://www.dtm.ciw.edu/users/nschmerr/site/Research.html

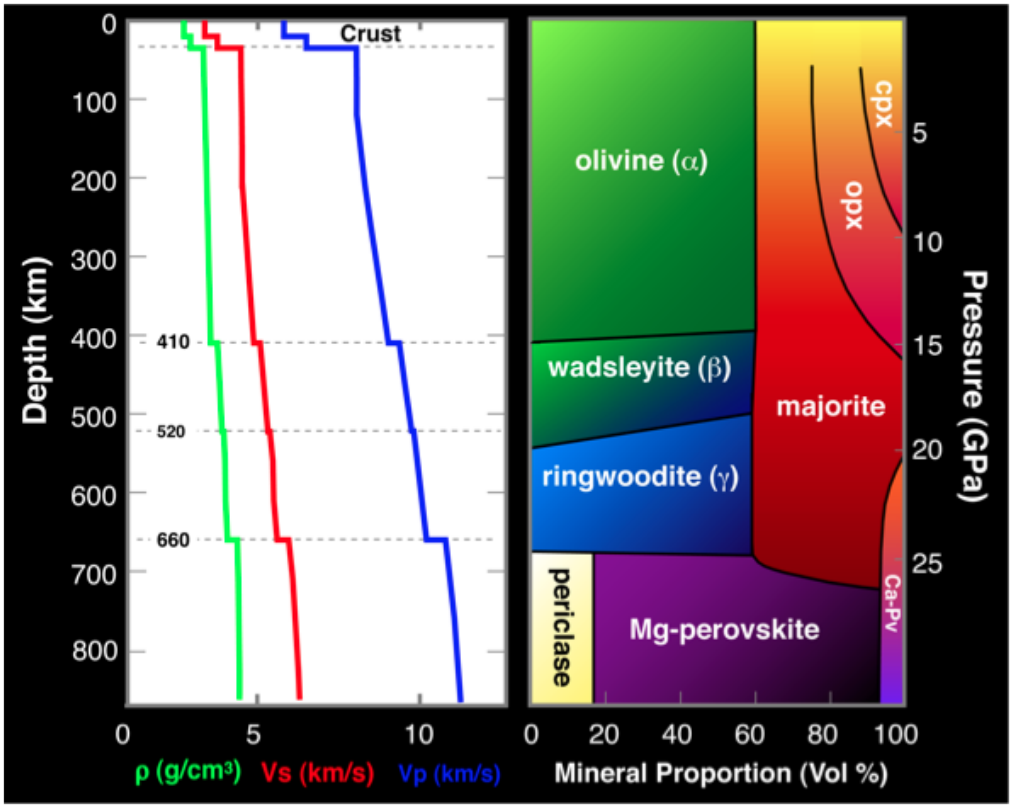

Figure 3. Rare Earth Element abundances in MORB and OIB.
OIB and MORB have distinct rare earth chemistry. MORB is depleted in rare elements as compared to OIB concentrations. Elements of increasing compatibility are preferentially partitioned into melt.

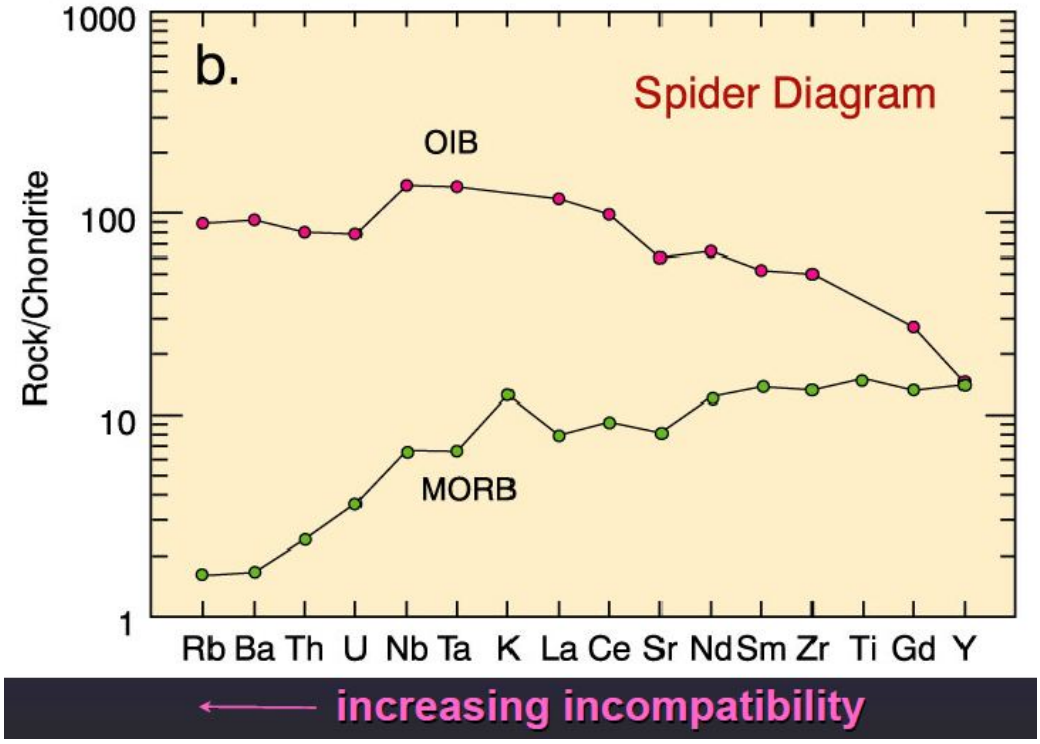

Figure 4. Layered vs. whole mantle convection.
Top: Layered mantle convection. Upper and lower mantle are distinct and un-mixing chemical reservoirs. Bottom: Whole mantle convection. There are no impenetrable layers acting as barriers to convection.
Source: http://faculty.plattsburgh.edu/mary.rodentice/

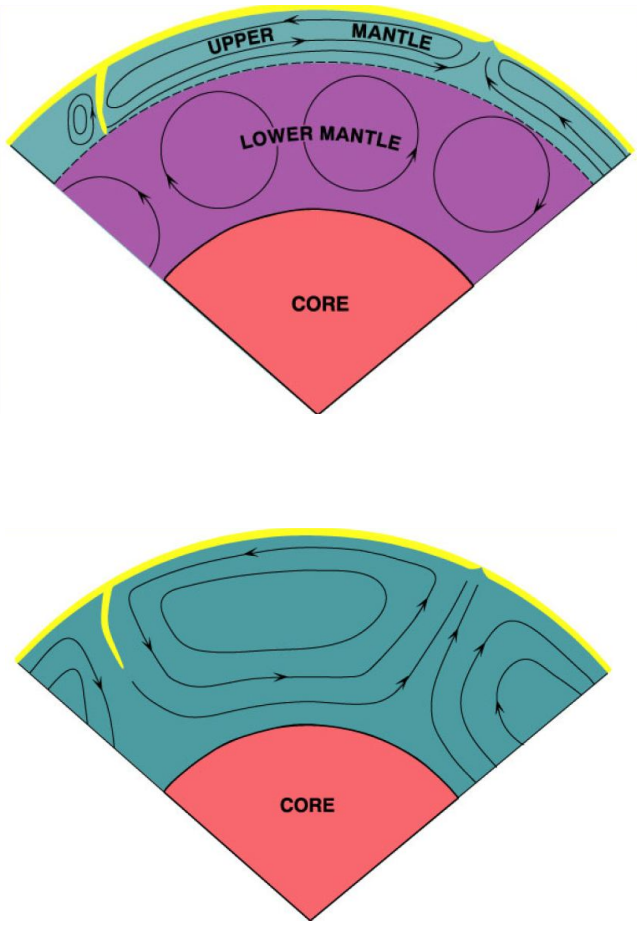

Figure 5. Cartoon of transition zone water filter model.
Hydrated transition zone material (wadsleyite) upwelling through the 410-km discontinuity partially melts during the phase transformation to olivine. Incompatible elements are filtered into the melt layer. The residuum continues to rise and becomes MORB source. Figure from Bercovici and Karato, 2003.

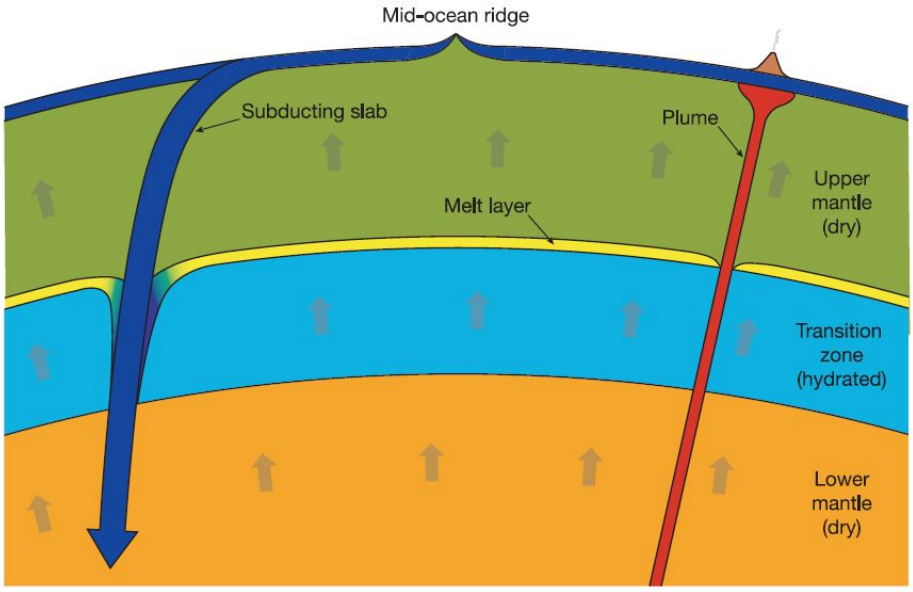

Figure 6. Seismic tomography images of subducting oceanic lithosphere
The blue regions are subducting oceanic lithosphere. In each inset figure oceanic lithosphere has penetrated the mantle transition zone. In the middle inset oceanic lithosphere has reached the core-mantle boundary.
Source: http://www.geotimes.org/july07/article.html?id=feature_deeper.html

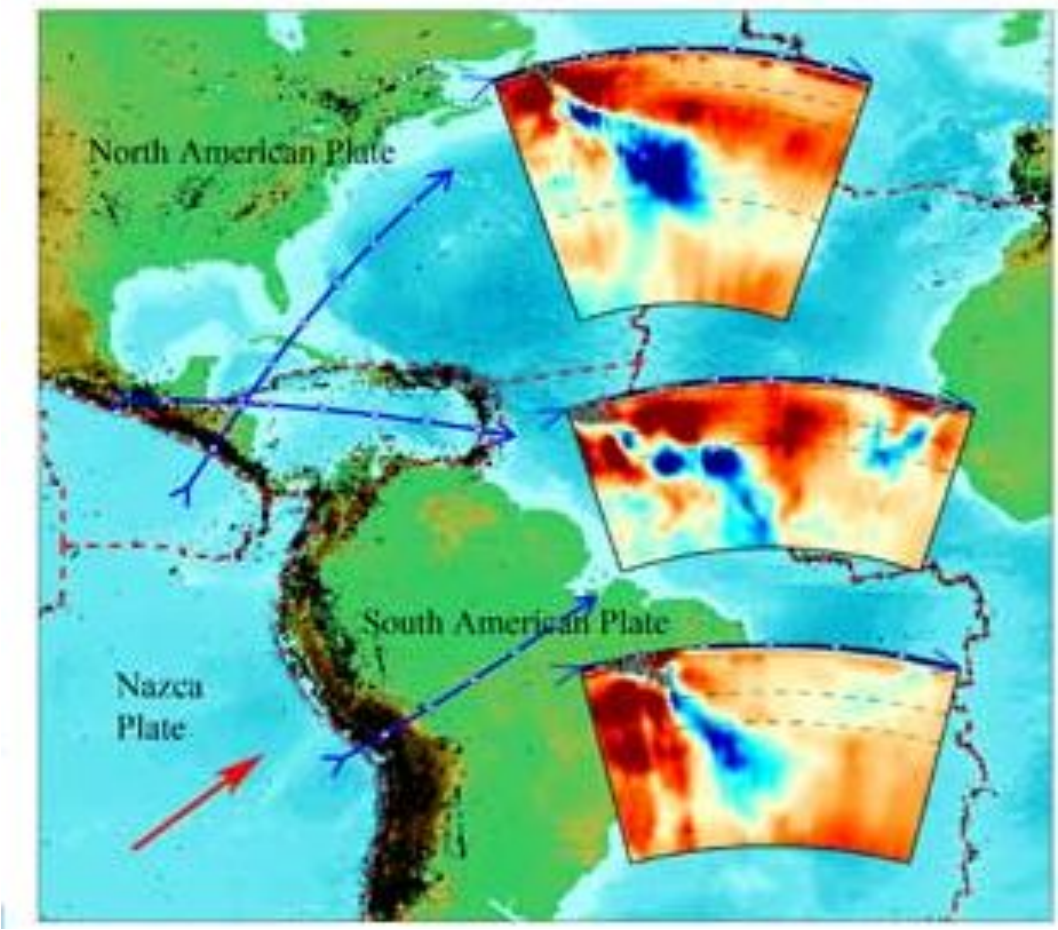

Figure 7. Cartoon of P-to-S conversion, receiver function time series, water level deconvolution.
Top: P-to-S conversion at the 410-km discontinuity. Middle: Receiver functions are a superposition of all P-to-S conversions at internal earth boundaries. Bottom: Water level regularization. In spectral division frequencies with spectral amplitude below a cutoff are normalized to the cutoff amplitude, thus stabilizing the spectral division.

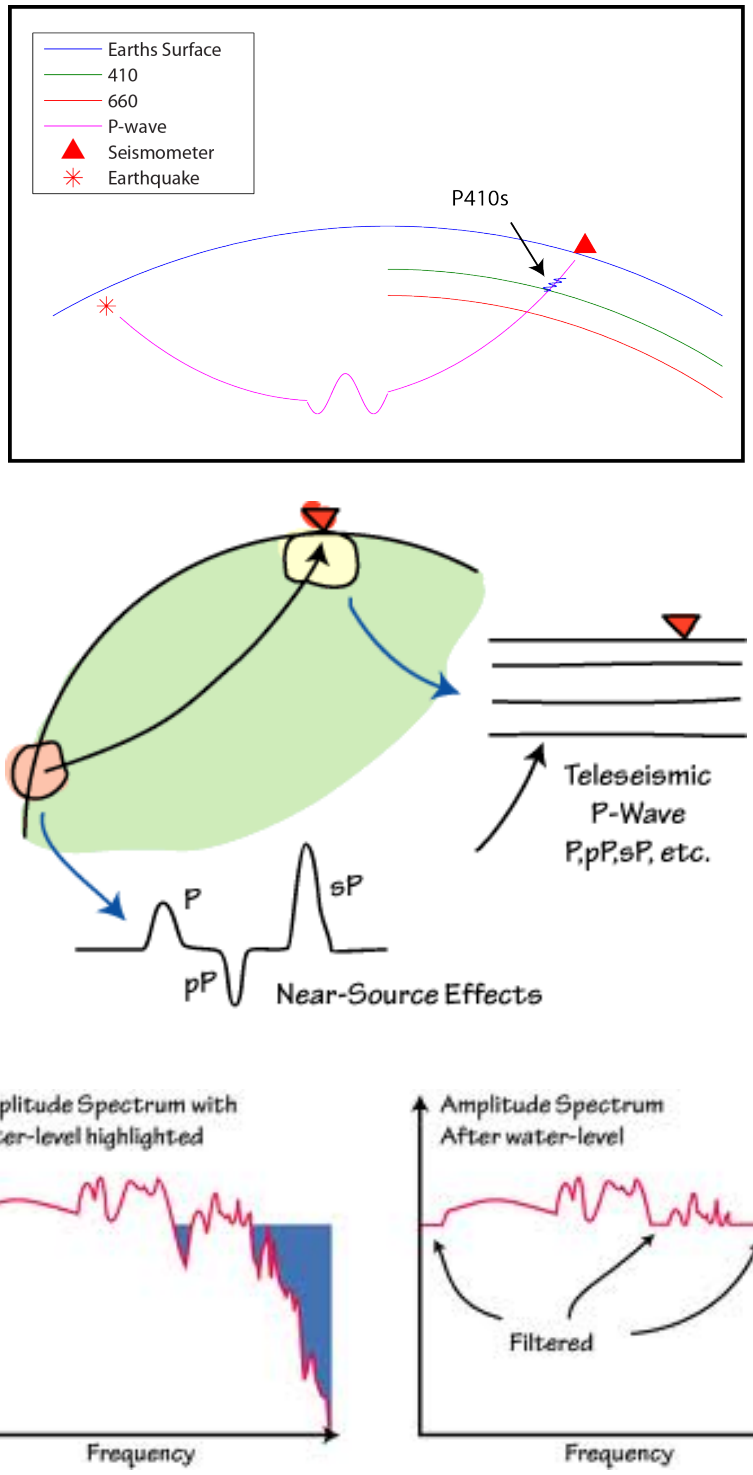

Figure 8. Seismic stations from Earthscope Transportable Array used in this study.

Seismic stations (*). Tucson, Arizona (black circle). Receiver calculated at these stations sample 410-km discontinuity beneath southeastern corner of Arizona.

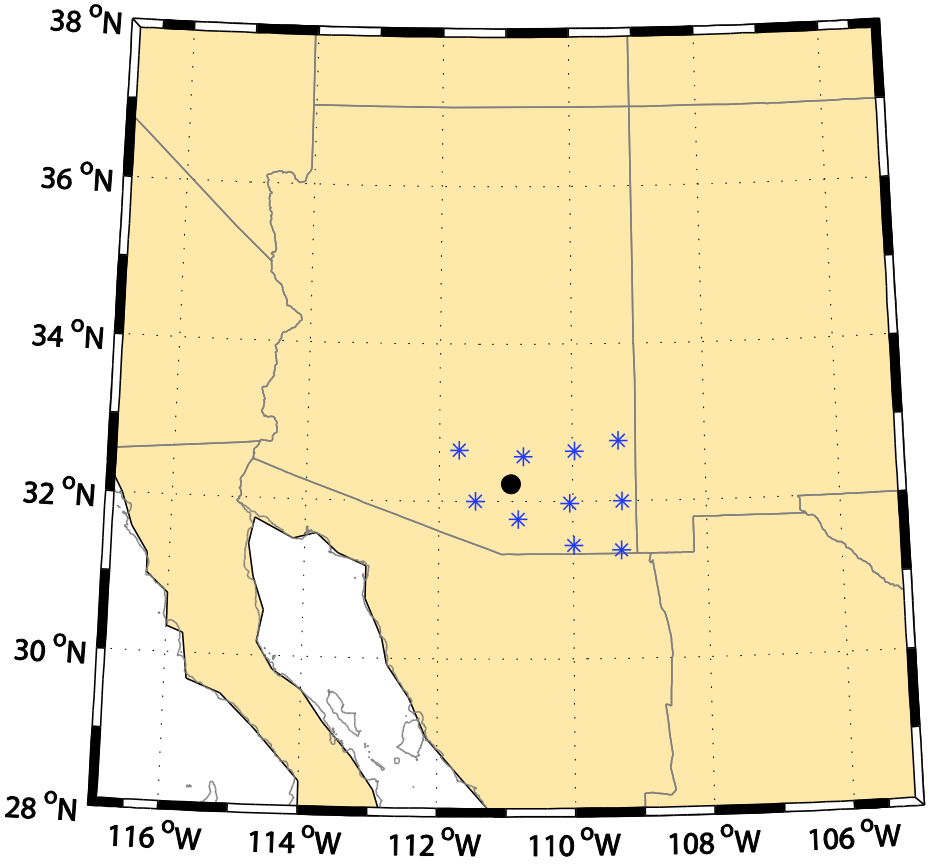

Figure 9. Distribution of earthquake sources relative to the seismic stations. Numbers on the outside edge are the back-azimuths (degrees) of each earthquake relative the geographic center of the array. Numbers along the radius of the circle are the epicentral distances (degrees) from each earthquake to the array.

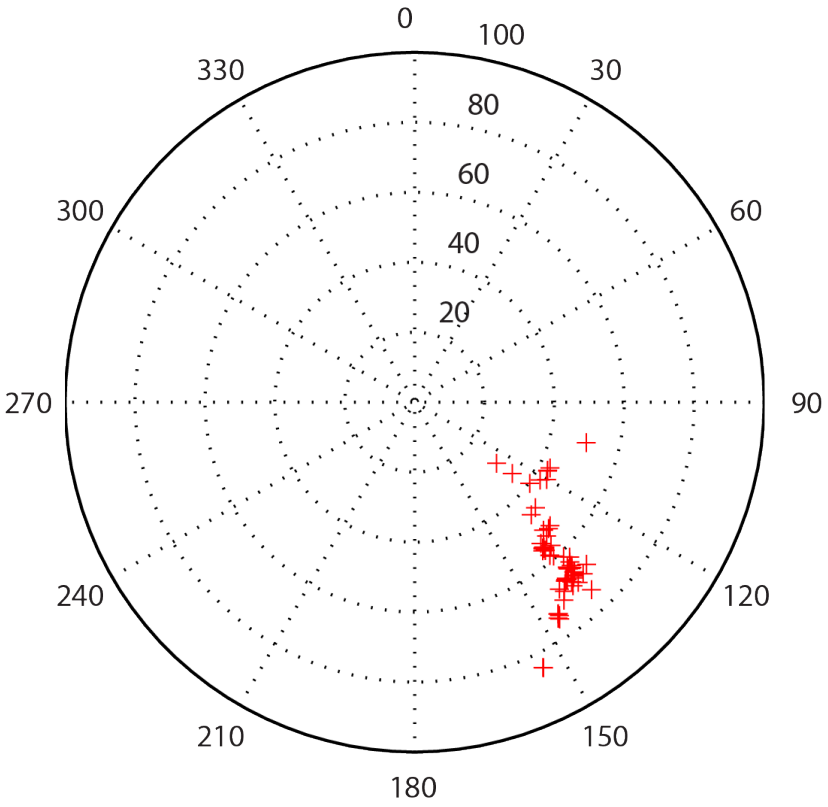

Figure 10. Linear stack of subsetted receiver functions.
The total set of all computed receiver functions (517) were culled to a final set of 396 receiver functions and were linearly stacked to produce an average receiver function response beneath the seismic stations. The P-to-S conversion at the 410-km discontinuity ($P_{410}s$) and the negative polarity P-to-S conversion at the low-velocity layer atop the 410 (410-LVL) are labeled.

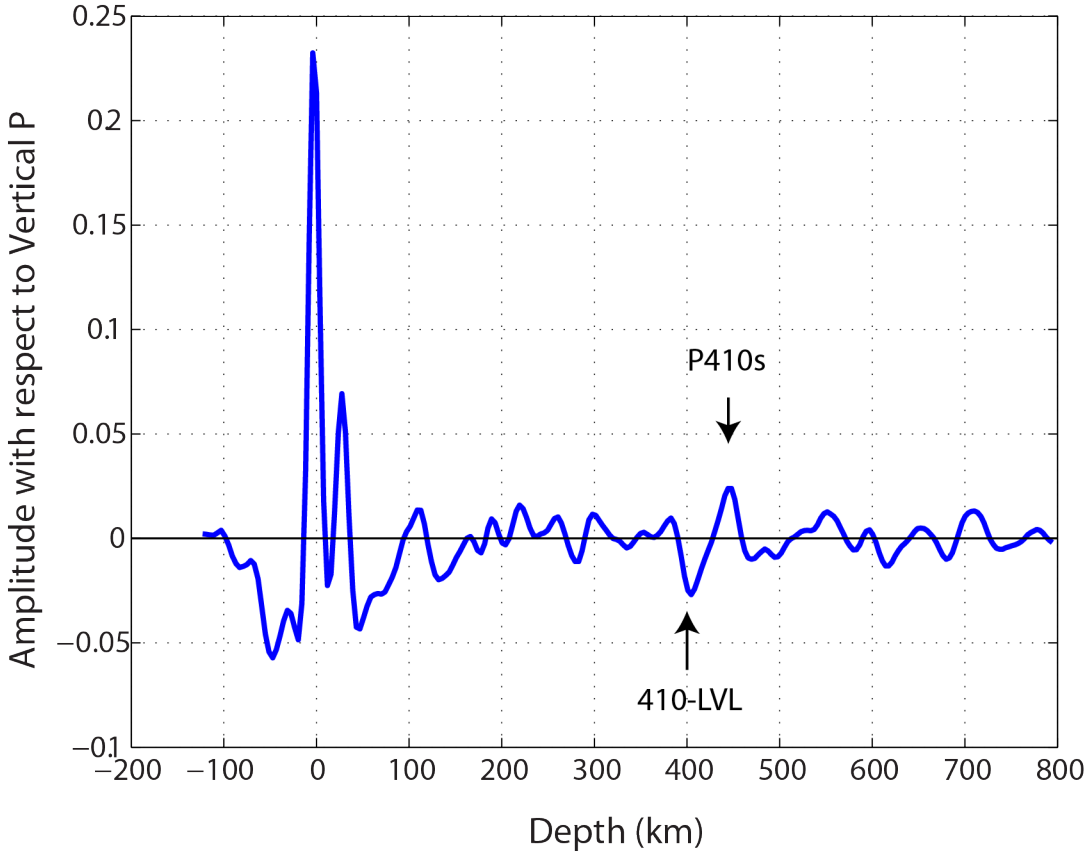

Figure 11. Parameterization of the double-gradient slab velocity model.
Black line: IASP91 shear velocity model. Red dash line: typical double gradient slab model. Synthetic receiver functions were computed from a 5 parameter velocity model, perturbing the IASP91 velocity model. TG: Top gradient thickness (km), BG: Bottom gradient thickness (km), ST: Slab thickness (km), dVs-TG: Shear wave velocity reduction in top gradient, dVs-BG: Shear wave velocity increase in the bottom gradient after recovering the model to IASP91. Parameter ranges are given in Table 1.

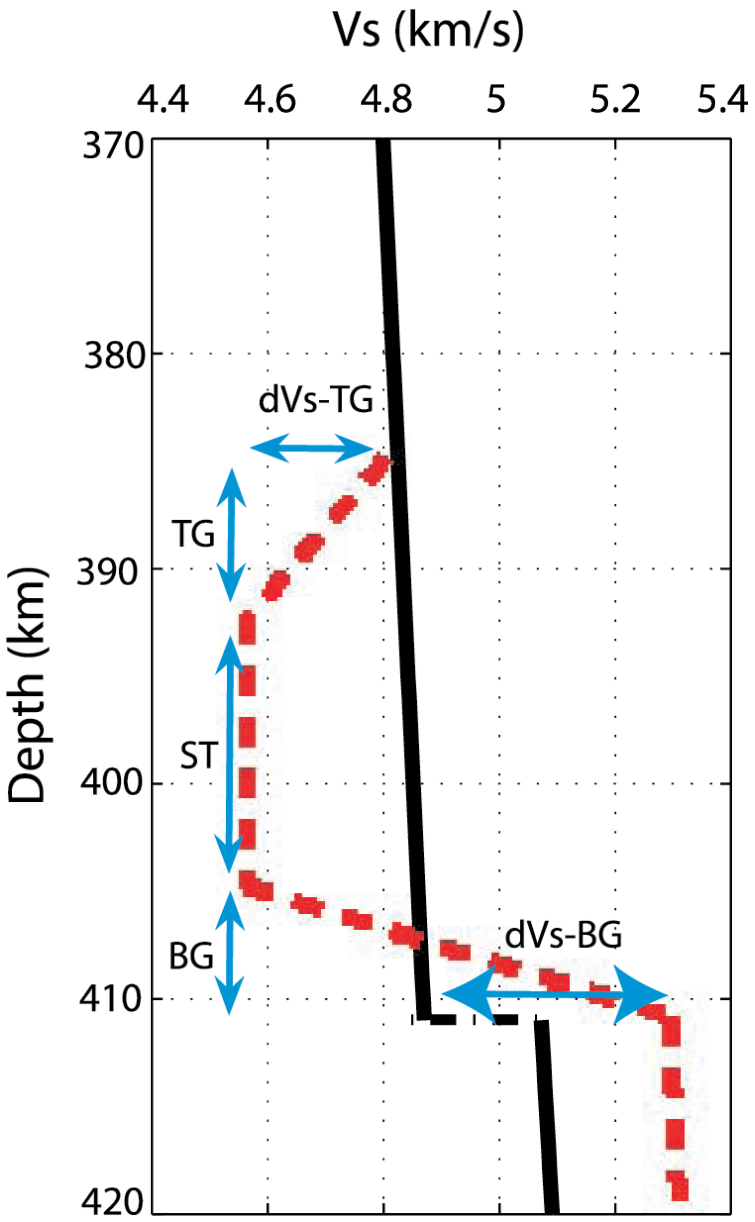

Figure 12. Best fitting synthetic receiver function to the observed data.
Red dashed lines: standard error bars of the mean receiver function show in Figure 10 zoomed to about the $P_{410}s$ arrival. Blue line: Best fitting synthetic receiver function from all double-gradient slab models.

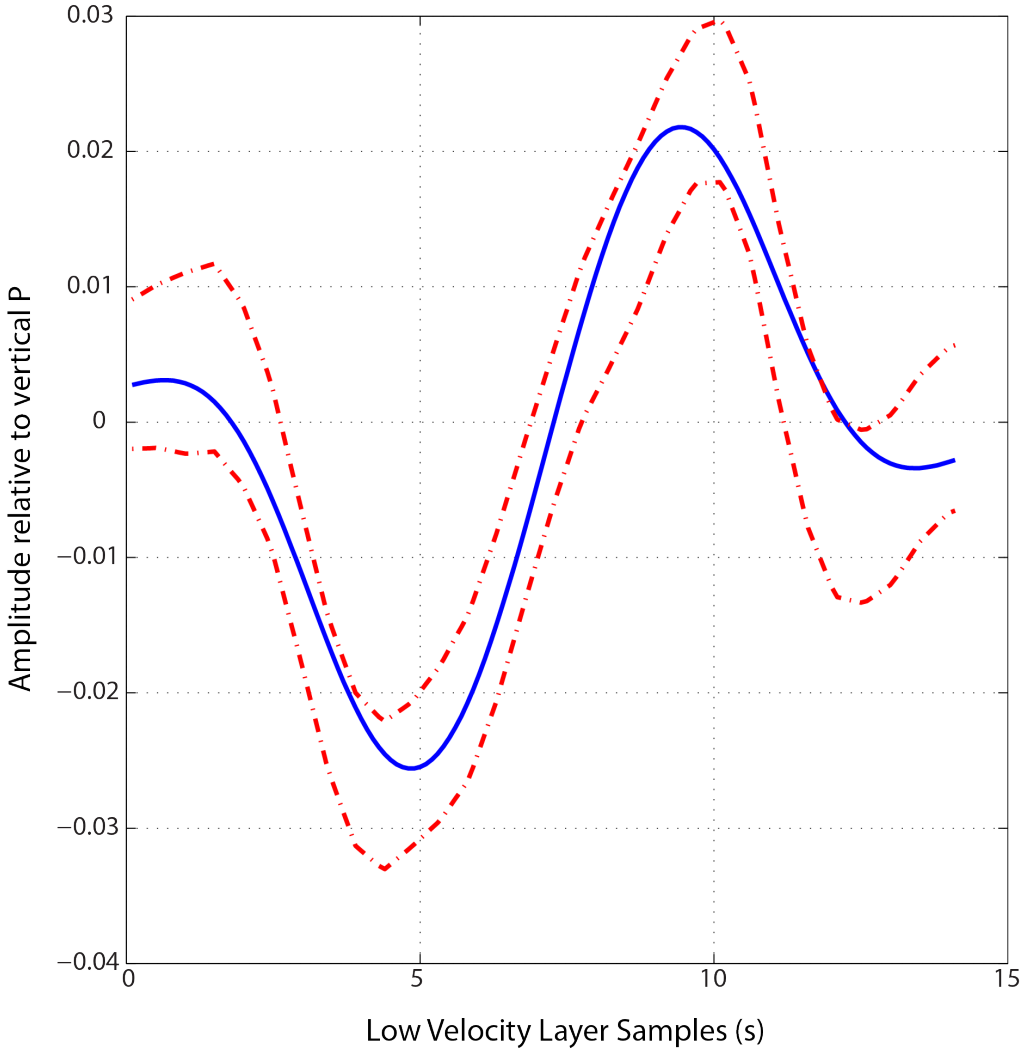

Figure 13. One- and two-dimensional marginal probability distributions of the five model parameters.

Main diagonal: One-dimensional marginal probability distributions for each model parameter. Peaks of the distributions indicate the most probable value for each parameter. Off diagonal plots: Two dimensional marginal probability distributions indicating tradeoffs in model fit between each pair of model parameters.

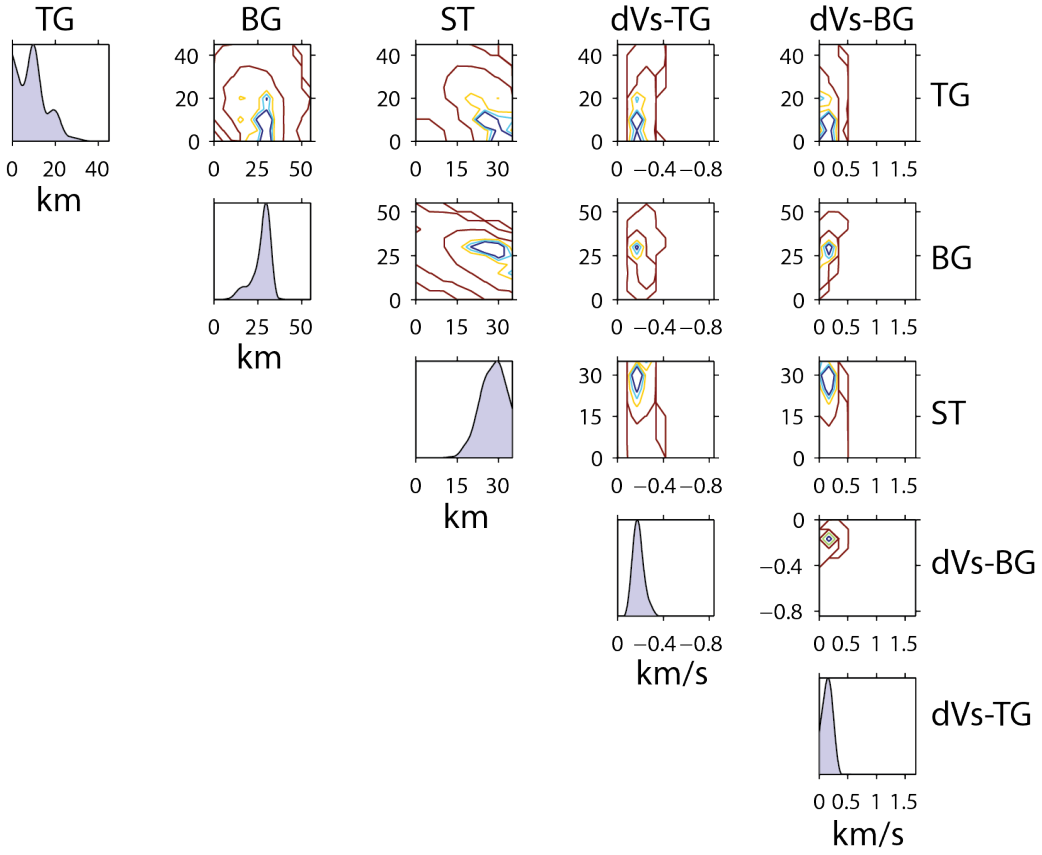

Figure 14. Best fitting double-gradient slab velocity model.
Best fitting model parameters are indicated alongside the plot of the best fitting DGS model. The model indicates a low velocity layer atop the 410-km seismic discontinuity and a diffuse olivine to wadsleyite phase transformation.

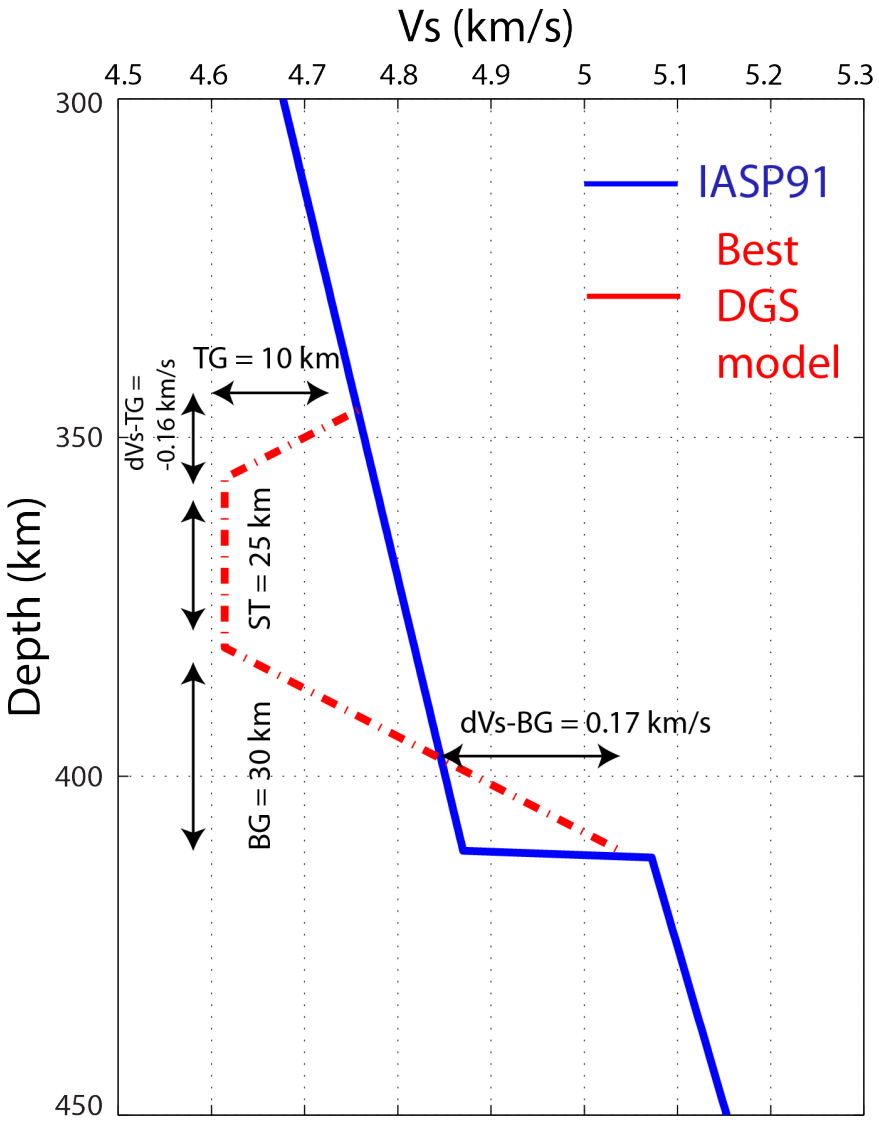

Table 1. Double gradient slab model parameter ranges.

TG (km)	**BG (km)**	**ST (km)**	**dV_s-TG (km/s)**	**dV_s-BG (km/s)**
0:5:45	0:5:35	0:5:55	-0.8:0.08:0	0:0.17:1.7